

# Absorbers for medical X-ray detectors with optimum spatial resolution: a simulation study

M. Hoheisel<sup>a</sup>, J. Giersch<sup>b</sup>, M. Mitschke<sup>b</sup>, and P. Bernhardt<sup>a</sup>

<sup>a</sup> Siemens AG Medical Solutions, Forchheim, Germany

<sup>b</sup> Physics Institute 4, University Erlangen-Nürnberg, Germany

## ABSTRACT

The requirements for medical X-ray detectors tend towards higher spatial resolution, especially for mammography. Therefore, we have investigated common absorber materials with respect to the possible intrinsic limitations of their spatial resolution.

Primary interaction of an incident X-ray quantum is followed by a series of processes: Rayleigh scattering, Compton effect, or the generation of fluorescence photons and subsequent electrons. Lateral diffusion of carriers relative to their drift towards the electrodes also broadens the point-spread function. One consequence is that the spatial resolution of the detector, expressed in terms of the modulation transfer function (MTF), is reduced.

Monte Carlo simulations have been carried out for spectra with tube voltages of 28 – 120 kV using the program ROSI (Roentgen Simulation) based on the well-established EGS4 algorithm. The lateral distribution of deposited energy has been calculated in typical materials such as Se, CdTe, HgI<sub>2</sub>, and PbI<sub>2</sub> and used to determine the line spread function.

The complex absorption process is found to determine the spatial resolution of the detector considerably. The spectrum at energies closely above the K-edge of the absorber material tends to result in a reduced MTF. At energies above 50 keV, electron energy loss increasingly reduces spatial resolution in the high frequency range. The influence of fluorescence is strongest in the 5 – 20 lp/mm range. If a very high spatial resolution is required, a well-adapted semiconductor should be applied.

Keywords: Medical X-ray imaging, detectors, absorber, photon counting, Monte Carlo simulation, modulation transfer function

## 1. INTRODUCTION

In the field of medical X-ray detectors, semiconductor-based flat-panel detectors have begun to replace conventional film-screen systems, storage phosphor plates, and image intensifier TV systems. The detectors consist of matrices of switches made from amorphous silicon thin-film transistors, coupled either to photodiodes to register the light emitted by a scintillator<sup>1</sup>, or to a directly absorbing semiconductor layer<sup>2</sup>. The signal is integrated over the pixel area, but photon counting is also feasible.

Some directly absorbing semiconductors exhibit an excellent spatial resolution even in relatively thick layers (e.g. 500  $\mu\text{m}$ ) because radiation-generated charge carriers have a lateral diffusion length which is small compared to their drift length. Indeed, spatial resolution is limited by intrinsic processes associated with X-ray scattering and absorption as well as energy loss of the generated electrons<sup>3</sup>.

Of course, the results have to be seen with respect to the requirements for medical X-ray detectors. For the imaging of soft tissue, resolutions from 0 to 2 lp/mm (line pairs per mm) are mandatory. For bones, even more than 3 lp/mm are favorable, and special applications such as dental radiography or mammography require 5 lp/mm up to 10 lp/mm<sup>4</sup>.

In this study we tried to take account of all effects: X-ray absorption, fast electron energy loss, electron hole pair generation, and charge carrier transport. The X-ray spectra used were similar to those commonly applied in medical diagnosis. A wide variety of semiconductor materials generally utilized for radiation detectors has been investigated.

## 2. METHOD

The signal-generating processes have been studied by Monte Carlo simulations using the program ROSI (Roentgen Simulation) written by Giersch et al.<sup>5</sup>. First orientating simulations were carried out at monochromatic energies in the range between 10 keV and 100 keV<sup>6</sup>.

The first simulation step is the X-ray interaction of the incident radiation with the absorber. Quanta can become elastically scattered (Rayleigh scattering), inelastically scattered (Compton scattering) where they lose energy and fast electrons are generated, or absorbed by a photoelectric process where fluorescence quanta as well as fast electrons are generated. The secondary quanta travel a certain distance and either leave the absorber or interact in a consecutive process. Thus, X-ray absorption takes place distributed in space.

The second simulation step is the energy loss of the fast electrons. They can be scattered either elastically or inelastically. In the latter process, multiple electron-hole pairs are excited. Thus, electron energy loss is also a process which leads to a signal generation distributed in space.

The excited charge carriers, in the case of a directly absorbing semiconductor, are collected by an electrical drift field. Moreover, carrier diffusion tends to distribute the signal in space. The ratio of diffusion length to drift length is relevant to tell how the signal is blurred by charge transport.

The signal is collected in a pixel, i.e. the signal is integrated over the active pixel area. In terms of modulation transfer function, the pixel size determines a sinc function  $\sin(x)/x$  as an upper limit for an ideal detector. Moreover, the signal is made ambiguous through the discrete sampling for spatial frequencies above the Nyquist frequency.

In the simulations an X-ray fan beam is directed onto the detector, which is assumed to consist of a 10  $\mu\text{m}$  wide pixel grid. The beam is slightly tilted (by 5°) to produce oversampling. An example for a resulting image is given in Fig. 1. From this image, we determine the presampled line spread function.

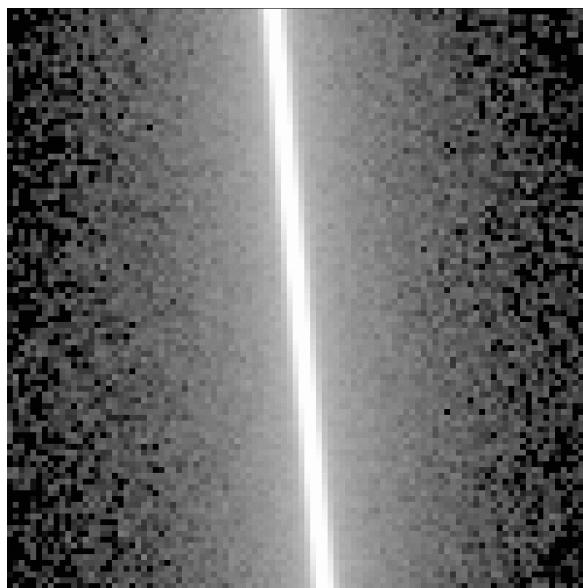
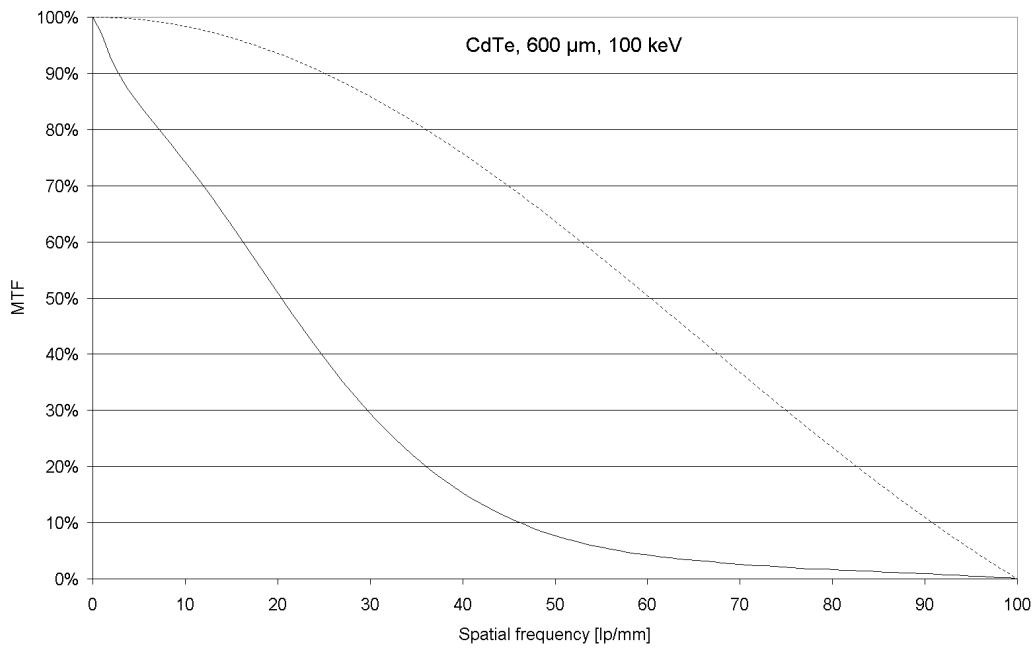


Figure 1: Simulated image of an infinitesimally thin X-ray fan beam, 100 keV, on a 600  $\mu\text{m}$  thick CdTe detector. Pixel size is 10  $\mu\text{m}$ .

Finally, we calculated the dependency of MTF on spatial frequency  $f$  (Fig. 2) using the program DQEVAL<sup>7</sup>. The MTF exhibits a continuous decay from 100% at 0 lp/mm down to 30% at 30 lp/mm. Above 50 lp/mm it flattens out. The sinc function

$$\text{sinc}(w f) = \frac{\sin(w \pi f)}{w \pi f} \quad (1)$$

for the chosen pixel size  $w$  of  $10\ \mu\text{m}$  is plotted for comparison. It marks the theoretical upper limit for the MTF.



**Figure 2:** Modulation transfer function (MTF) determined from the image of Fig. 1 compared to the sinc function related to a pixel size of  $10\ \mu\text{m}$  (dotted line).

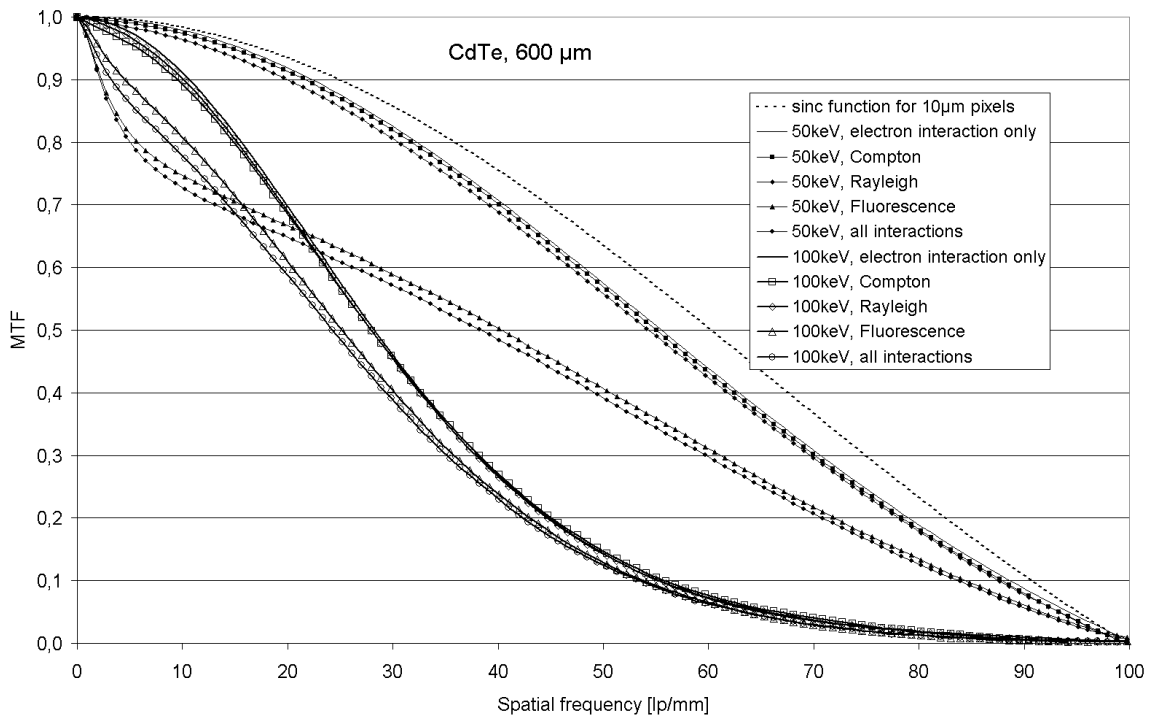


**Figure 3:** Modulation transfer function of a  $600\ \mu\text{m}$  CdTe layer for 50 and 100 keV considering only electron interaction, electron interaction together with the Compton effect, the Rayleigh effect, or fluorescence, respectively, and all interactions. The sinc function (dotted line) is plotted for comparison.

For a better understanding of the impact of the different interactions, simulations of the processing cascade have been performed where each process could be “switched on” and “switched off” individually. Figure 3 shows the resulting MTF curves for the monochromatic energies of 50 keV and 100 keV obtained at a 600  $\mu\text{m}$  thick CdTe layer.

At 50 keV, the interaction of fast electrons generated by the photo effect reduces the MTF below the limiting curve given by the sinc function. Adding the Compton or the Rayleigh effect has only a minor influence on the spatial resolution. However, including fluorescence leads to a pronounced drop in the MTF even at 5 lp/mm, i.e. fluorescence quanta have a long range in the order of 200  $\mu\text{m}$ . At 100 keV, electron ranges are in the order of 30  $\mu\text{m}$  and, therefore, their interaction diminishes the MTF drastically. Again, the Compton and Rayleigh effects have little influence, but fluorescence further reduces the MTF.

In this study we have used 6 typical spectra, which have been generated according to the algorithms published by Boone<sup>8</sup> and listed in Table 1. They span the whole energy range of medical diagnostic procedures.

Table 1

No.	Case	X-ray source and prefiltration	Tube voltage	Phantom	Mean energy
#1	Mammography 4 cm breast phantom	Mo anode 1 mm Be window 30 $\mu\text{m}$ Mo prefiltration	28 kV	4 mm AP6 32 mm BR12 4 mm AP6 1 mm PMMA	17.5 keV
#2	Mammography 8 cm breast phantom	W anode 1 mm Be window 50 $\mu\text{m}$ Rh prefiltration	35 kV	4 mm AP6 72 mm BR12 4 mm AP6 1 mm PMMA	23 keV
#3	Radiography 10 cm water phantom	W anode 2 mm Al window 0.2 mm Cu prefiltration	55 kV	5 mm PMMA 90 mm water 5 mm PMMA	41 keV
#4	Radiography 20 cm water phantom	W anode 2 mm Al window 0.2 mm Cu prefiltration	70 kV	5 mm PMMA 190 mm water 5 mm PMMA	47 keV
#5	Radiography 30 cm water phantom	W anode 2 mm Al window 0.2 mm Cu prefiltration	100 kV	5 mm PMMA 290 mm water 5 mm PMMA	59 keV
#6	Computed tomography 32 cm water phantom	W anode 2.5 mm Al window 1.2 mm Ti prefiltration	120 kV	5 mm PMMA 310 mm water 5 mm PMMA	65 keV

Several materials have been investigated, namely the scintillators  $\text{Gd}_2\text{O}_2\text{S}$  and CsI, the elementary semiconductors Si, Ge, and Se, and compounds such as GaAs, CdTe,  $\text{HgI}_2$ , PbO,  $\text{PbI}_2$ , and TlBr. The layer thicknesses  $d$  were 200  $\mu\text{m}$  for the spectra #1 and #2, and 600  $\mu\text{m}$  for the higher energies.

Although the X-ray properties of the scintillators CsI and  $\text{Gd}_2\text{O}_2\text{S}$  have been studied, they will be disregarded in the following. For a detailed investigation of the spatial resolution it would have been necessary to simulate the optical behavior of these materials also, which is rather complicated and not within the scope of this study.

Starting from the carrier mobility  $\mu$  in a semiconductor, the transit time  $t_{\text{tr}}$  and diffusion constant  $D_{\text{diff}}$  can be calculated from

$$t_{\text{tr}} = \frac{d^2}{\mu U} \quad (2)$$

and

$$D_{\text{diff}} = \frac{\mu kT}{e} \quad (3)$$

leading to a diffusion length  $L_{\text{diff}}$

$$L_{\text{diff}} = \sqrt{D_{\text{diff}} t_{\text{tr}}} = \sqrt{\frac{kT d^2}{e U}} \quad (4)$$

$L_{\text{diff}}$  is independent of material properties and depends only on layer thickness and applied voltage. The drift voltages  $U$  applied to the semiconductor layers and the resulting diffusion lengths  $L_{\text{diff}}$  have been compiled in Table 2. All  $L_{\text{diff}}$  values have been computed from eqn. (4) for room temperature except the value for Ge, where cooling down to 77 K has been assumed.

Table 2

Semiconductor (data source)	Layer thickness [ $\mu\text{m}$ ]	Drift voltage [V]	Electrical field [V/ $\mu\text{m}$ ]	Diffusion length [ $\mu\text{m}$ ]
CdTe <sup>9</sup>	200	10	0.05	10.17
	600	30		17.61
GaAs <sup>10</sup>	200	200	1.00	2.27
	600	600		3.94
Ge <sup>11</sup>	200	60	0.30	2.10
	600	180		3.64
HgI <sub>2</sub> <sup>12</sup>	200	40	0.20	5.08
	600	120		8.81
PbI <sub>2</sub> <sup>13</sup>	200	267	1.33	1.97
	600	800		3.41
PbO <sup>14</sup>	200	600	3.00	1.31
	600	1800		2.27
Se <sup>15</sup>	200	2000	10.00	0.72
	600	6000		1.25
Si <sup>16</sup>	200	67	0.33	3.94
	600	200		6.82
TlBr <sup>17</sup>	200	87	0.43	3.45
	600	261		5.97

We estimate charge carrier propagation in a simple model as follows. The carriers are assumed to diffuse laterally during their drift through the semiconductor into a cone-shaped volume with a width given by the diffusion length  $L_{\text{diff}}$ . This will result in a triangular shaped broadening of the line spread function. Thus the MTF has to be multiplied with an additional sinc<sup>2</sup> factor.

$$\text{sinc}^2(L_{\text{diff}} f) = \left( \frac{\sin(L_{\text{diff}} \pi f)}{L_{\text{diff}} \pi f} \right)^2 \quad (5)$$

According to eqn. (4), the reduction of the MTF by lateral carrier diffusion is mainly determined by the applied electrical field. The relation is valid in the regime where the semiconductor is fully depleted and the carrier mobility is independent of the electric field<sup>18</sup>. A high field is favorable, but also causes an increased dark current. This restricts the possible bias voltage.

### 3. RESULTS

Due to the large amount of simulation data, only some selected results can be displayed here. Figure 4 shows the MTF curves obtained for a Se layer, taking account of all X-ray and electron energy loss interactions.

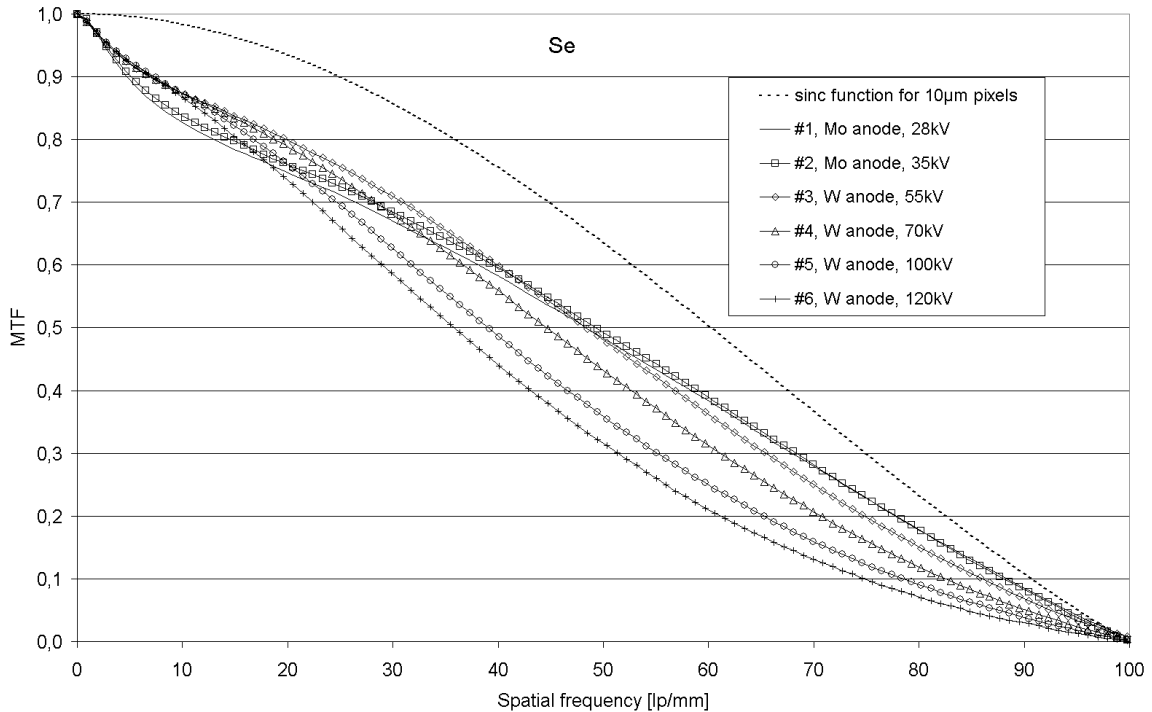


**Figure 4:** Modulation transfer function for 6 different spectra according to Table 1 calculated for a Se absorber (thickness for #1 and #2 is 200  $\mu\text{m}$ , else 600  $\mu\text{m}$ ). All X-ray interactions have been included. The sinc function (dotted line) is plotted for comparison.

All curves run markedly lower than the sinc function, which has been plotted for comparison as the theoretical upper limit. At spatial frequencies below 20 lp/mm, spectrum #1 (Mo anode, 28 kV) delivers the lowest MTF values. This can be explained by the spectrum being just above the K-edge energy of Se (12.7 keV). At higher spatial frequencies the MTF curves tend to become lower with increasing energy, which reflects the features demonstrated above (Fig. 3).

In Figure 5, the MTF curves of 9 different materials are compiled for spectrum #1 (Mo anode, 28 kV, see Table 1). The influence of transport has been neglected in this graph. The lowest curves are those of Se, Ge, and GaAs with K-edge energies of 12.7 keV, 11.1 keV, and 10.4 keV or 11.9 keV, respectively. In these cases the X-ray spectrum is just above the K-edge. With a K-edge far below the spectrum (Si 1.8 keV) or above it (Te 31.8 keV, I 33.2 keV, Hg 83.1 keV, Tl 85.5 keV, Pb 88 keV), the MTF reaches nearly the theoretical limit, which is given by the sinc function (dotted line).

In Figure 6, the MTF curves of 9 different materials are compiled for the spectrum with the highest energy, spectrum #6 (W anode, 120 kV, see Table 1). Again, the influence of transport has been neglected. Here, the lowest curve comes from Si, where the energy loss of fast electrons is relatively small because of its low mass density. The electron range becomes wide enough to diminish the MTF. All other materials lead to MTF curves which deviate markedly from the sinc function (dotted line).

All other simulation data not shown in this paper resulted in sets of curves between the two extreme cases of Fig. 5 and Fig. 6.

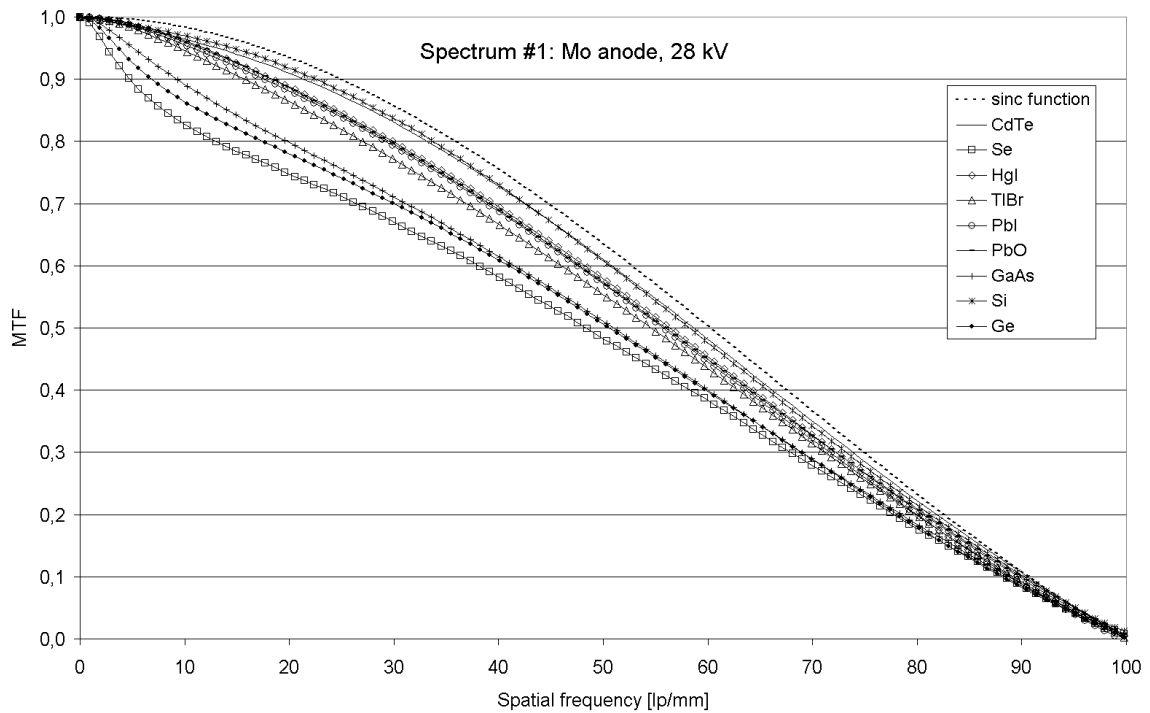


**Figure 5:** Modulation transfer function for spectrum #1 (Mo anode, 28 kV) according to Table 1 calculated for different semiconductors. All X-ray interactions have been included, only transport has been ignored. The sinc function (dotted line) is plotted for comparison.

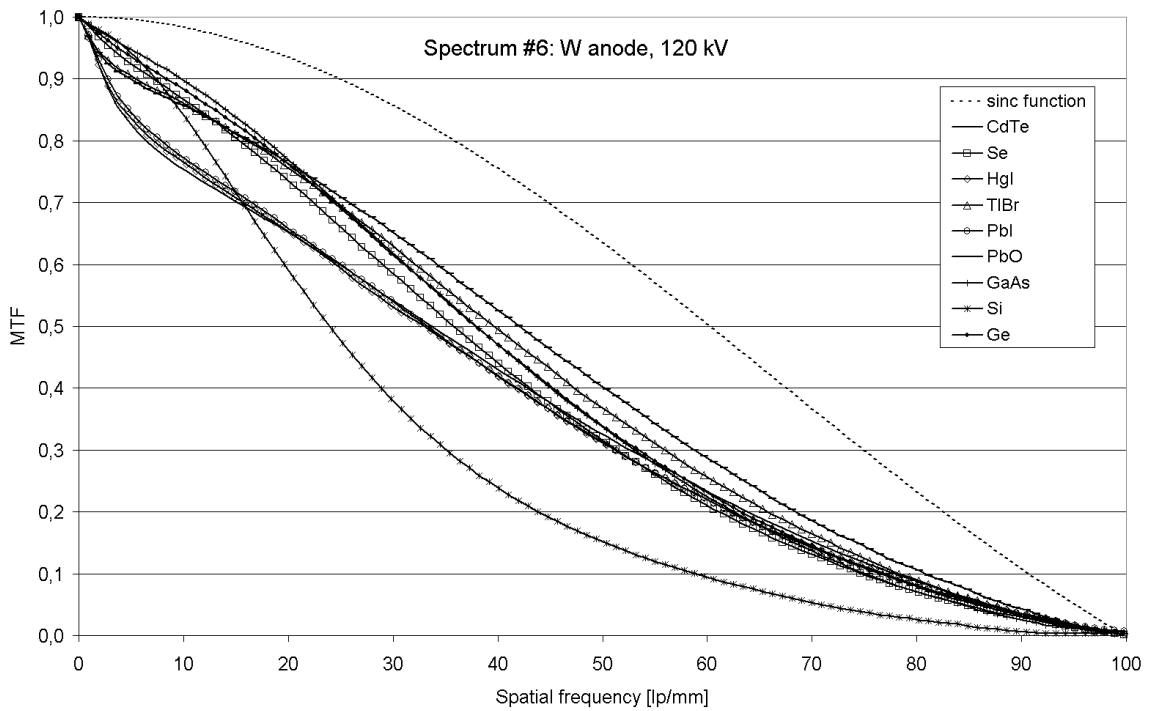


**Figure 6:** Modulation transfer function for spectrum #6 (W anode, 120 kV) according to Table 1 calculated for different semiconductors. All X-ray interactions have been included, only transport has been ignored. The sinc function (dotted line) is plotted for comparison.

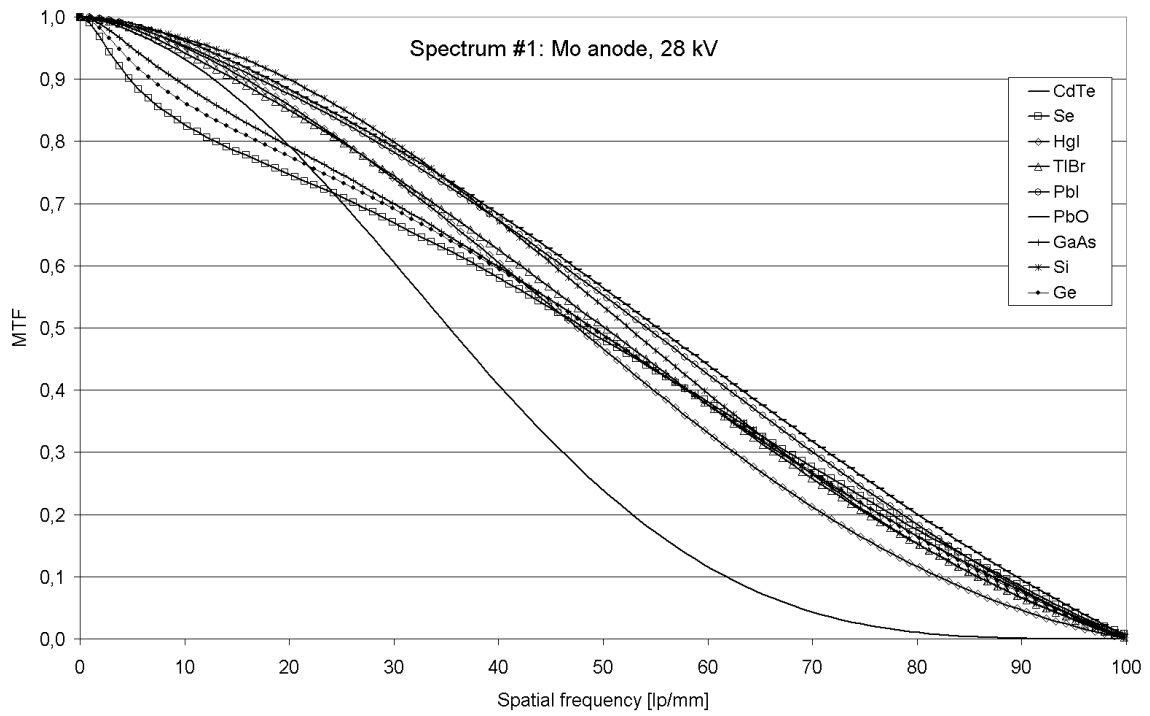


**Figure 7:** Modulation transfer function for spectrum #1 (Mo anode, 28 kV) according to Table 1 calculated for different semiconductors. All X-ray interactions and carrier transport have been taken into account.

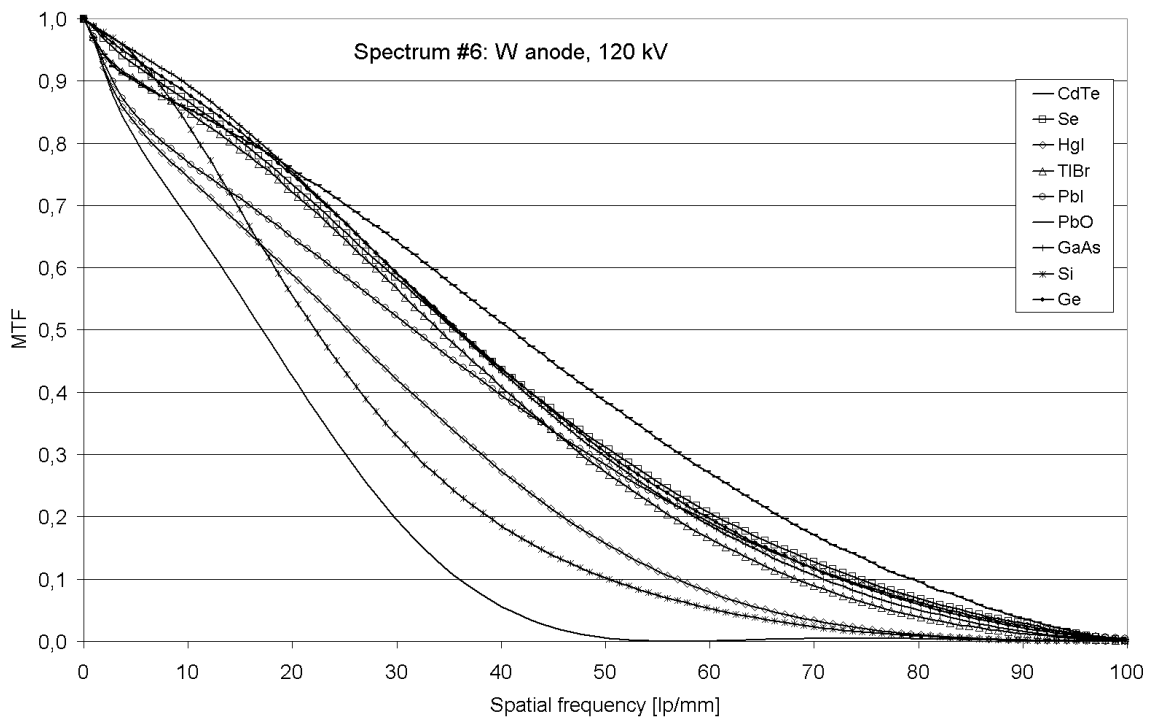


**Figure 8:** Modulation transfer function for spectrum #6 (W anode, 120 kV) according to Table 1 calculated for different semiconductors. All X-ray interactions and carrier transport have been taken into account.

The curves change when transport phenomena are also taken into account (Fig. 7 and 8). In the semiconductors investigated, carrier diffusion leads to a more or less pronounced lateral spreading of the signal. This affects the MTF. Nevertheless, this effect is not very strong in those semiconductors which allow a high drift field ( $> 0.4 \text{ V}/\mu\text{m}$ ) to be applied. If the drift voltage has to be kept low to prevent excessive dark currents, the MTF is reduced as can be seen in Fig.9 from direct comparison of simulations with and without carrier transport. The semiconductor was a  $600 \mu\text{m}$  thick CdTe layer biased with 30 V.

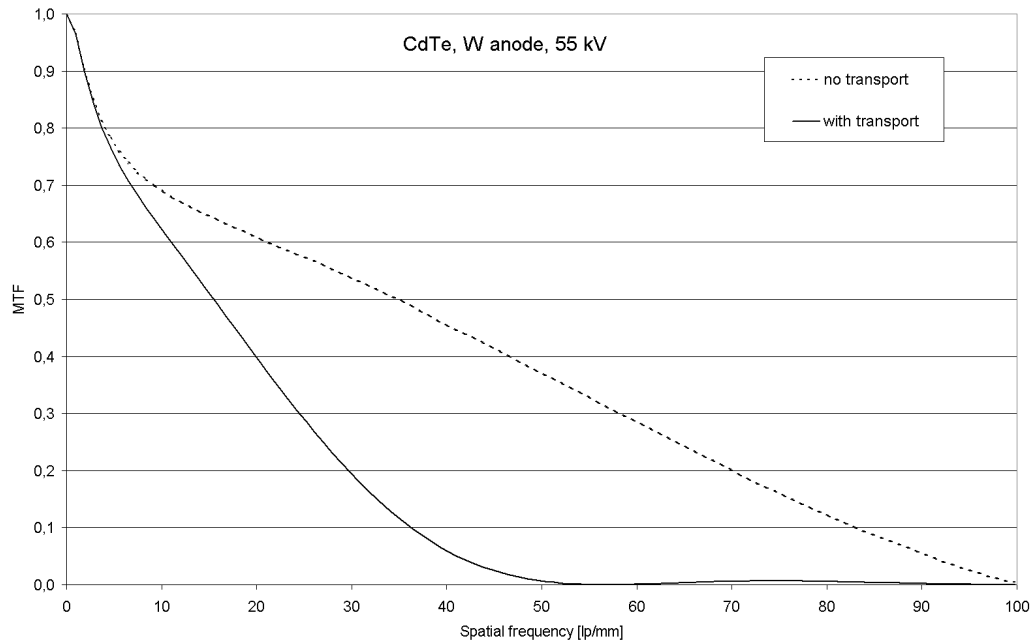


Figure 9: Modulation transfer function for spectrum #3 (W anode, 55 kV) according to Table 1 calculated for CdTe under  $0.05 \text{ V}/\mu\text{m}$  bias. All X-ray interactions with (solid line) or without (dotted line) carrier transport have been taken into account.

#### 4. CONCLUSIONS

Based on the results from this simulation study, if a detector with high spatial resolution is required for a specific application, the absorber material should be adapted to the X-ray spectrum used. The maximum of the spectrum is to be placed at an energy where the MTF of the favored absorber is high.

An interesting observation is that the strongest MTF decrease is found just above the K-edge, i.e. at an energy where the absorption has its highest value<sup>5</sup>. This might have an influence on the selection of the absorber material. But in most cases, high absorption is more important than high spatial resolution. Every percent of additional absorption allows the reduction of the radiation dose for a diagnostic procedure. A slightly reduced MTF can be accepted in the majority of cases.

The results demonstrate that the transport properties of the absorbing semiconductor layer, particularly the carrier diffusion length, also influence the spatial resolution of the radiation detector.

With respect to the X-ray properties, the scintillators CsI and  $\text{Gd}_2\text{O}_2\text{S}$  are also well qualified for detection. Admittedly, they have not been studied in detail within this work.

It also has to be pointed out that the simulations have been carried out up to 100 lp/mm. The relevant spatial frequencies for medical diagnosis are much lower (0 to 5 lp/mm, see above). Therefore, the MTF reduction found in this investigation can be tolerated in many cases. It should be kept in mind that the pixel size has a major influence on the resulting MTF. Moreover, to yield a detector with even higher spatial resolution, the individual pixels could be separated mechanically or by etching instead of using a contiguous semiconductor layer.

All absorber materials used in today's X-ray detectors operate far from their fundamental spatial resolution limits. Se has already proven its value in detectors for mammography<sup>2</sup>. CdTe (as well as CdZnTe which has related properties) is discussed for quanta counting detectors<sup>19</sup>. PbO, PbI<sub>2</sub>, HgI<sub>2</sub>, and TlBr are materials where dark currents, production processes and long-term stability are still open issues. Ge is at a disadvantage because it needs cooling. GaAs can hardly be produced on large areas and is thus too expensive. Si can be ruled out in most cases because of its poor X-ray absorption for medical spectra.

In summary we conclude that even if extremely high resolutions far beyond today's mammography and radiography applications are required, semiconductors of the type investigated here are very suitable materials.

## REFERENCES

1. M. Hoheisel, M. Arques, J. Chabbal, C. Chaussat, T. Ducourant, G. Hahm, H. Horbaschek, R. Schulz, M. Spahn, "Amorphous Silicon X-Ray Detectors", *Journal of Non-Crystalline Solids* **227-230**, 1300-1305, 1998
2. J. G. Yorker, L. S. Jeromin, D. L. Y. Lee, E. F. Palecki, K. P. Golden, Z. Jing, "Characterization of a full field digital mammography detector based on direct x-ray conversion in selenium", *Proceedings of the SPIE* **4682**, 21-29, 2002
3. G. Hajdok, J. J. Battista, I. A. Cunningham, "Fundamental limitations imposed by X-ray interactions on the modulation transfer function of existing X-ray detectors", *Proceedings of SPIE* **5030**, 1-15, 2003
4. M. Hoheisel, L. Bätz, "Requirements on amorphous semiconductors for medical X-Ray detectors", *Thin Solid Films* **383**, 132-136, 2001
5. J. Giersch, A. Weidemann, G. Anton, "ROSI – An object-oriented and parallel-computing Monte Carlo simulation for X-ray imaging", *Nuclear Instruments and Methods in Physics Research A* **509**, 151-156, 2003
6. M. Hoheisel, J. Giersch, P. Bernhardt, "Intrinsic Spatial Resolution of Semiconductor X-ray Detectors: A Simulation Study", *Nuclear Instruments and Methods in Physics Research A*, 2003, in press
7. L. Bätz, "Evaluation of the Modulation Transfer Function of a Digital X-ray Detector from Recorded Images of Bar Pattern Grids", internal report (unpublished), 2001
8. J. M. Boone, "Spectral modeling and compilation of quantum fluence in radiography and mammography", *Proceedings of the SPIE* **3336**, 592-601, 1998
9. E. Perillo, N. Auricchio, E. Caroli, A. Donati, W. Dusi, P. Fougères, M. Hage-Ali, G. Landini and P. Siffert, "Spectroscopic performance of newly designed CdTe detectors", *Nuclear Instruments and Methods in Physics Research A* **458**, 233-241, 2001
10. A. Owens, H. Andersson, M. Bavdaz, C. Erd, T. Gagliardi, V. Gostilo, N. Haack, M. Krumrey, V. Lämsä, D. Lumb, I. Lisjutin, I. Major, S. Nenonen, A. Peacock, H. Sipila, S. Zatoloka, "Development of compound semiconductor detectors for X- and gamma-ray spectroscopy", *Proceedings of the SPIE* **4784**, 244-258, 2002
11. Eurysis Mesures, Germanium Detector EGP 25-05, Operating Manual, Lingolsheim Cedex, France, 1996
12. R. A. Street, S. E. Ready, K. V. Schuylenbergh, J. Ho, J. B. Boyce, P. Nylen, K. Shah, L. Melekhov and H. Hermon, "Comparison of PbI<sub>2</sub> and HgI<sub>2</sub> for direct detection active matrix X-ray image sensor", *Journal of Applied Physics* **91**, 3345-3355, 2002
13. K. S. Shah, F. Olschner, L. P. Moy, P. Bennett, M. Misra, J. Zhang, M. R. Squillante, J. C. Lund, "Lead iodide X-ray detection systems", *Nuclear Instruments and Methods in Physics Research A* **380**, 266-270, 1996
14. A. Brauers, N. Conrads, G. Frings, U. Schiebel, M. J. Powell, C. Glasse, "X-ray sensing properties of a lead oxide photoconductor combined with an amorphous silicon TFT array", *Mat. Res. Soc. Symp. Proc.* **507**, 321-326, 1998
15. J. A. Rowlands, G. DeCrescenzo, N. Araj, "X-ray imaging using amorphous selenium: Determination of X-ray sensitivity by pulse height spectroscopy", *Medical Physics* **19**, 1065-1069, 1992
16. C. Ponchut, J. L. Visschers, A. Fornaini, H. Graafsma, M. Maiorino, G. Mettievier and D. Calvet, "Evaluation of a photon-counting hybrid pixel detector array with a synchrotron X-ray source", *Nuclear Instruments and Methods in Physics Research A* **484**, 396-406, 2002
17. K. Hitomi, M. Matsumoto, O. Muroi, T. Shoji, Y. Hiratate, "Characterization of thallium bromide crystals for radiation detector applications", *Journal of Crystal Growth* **225**, 129-133, 2001
18. H. G. Spieler, E. E. Haller, "Assessment of present and future large-scale semiconductor detector systems", *IEEE Transactions on Nuclear Science*, **NS-32**, 419-426, 1985
19. P. J. Sellin, "Recent advances in compound semiconductor radiation detectors", *Nuclear Instruments and Methods in Physics Research A* **513**, 332-339, 2003